Langmuir Article

pubs.acs.org/Langmuir

Atomic Force Microscopy Characterization of Cellulose Nanocrystals

Roya R. Lahiji,*[,†,‡] Xin Xu,[†,§] Ronald Reifenberger,[†,‡] Arvind Raman,[†,§] Alan Rudie,[⊥] and Robert J. Moon*[,†,∥,⊥]

[†]*Birck Nanotechnology Center,* [‡]*Department of Physics,* [§]*School of Mechanical Engineering, and* [∥]*School of Materials Engineering, Purdue University, 1205 W. State Street, West Lafayette, Indiana 47907-2057, and* [⊥]*US Forest Service, Forest Products Laboratory, 1 Gifford Pinchot Drive, Madison, Wisconsin 53726-2398*

Received September 17, 2009. Revised Manuscript Received November 25, 2009

Cellulose nanocrystals (CNCs) are gaining interest as a "green" nanomaterial with superior mechanical and chemical properties for high-performance nanocomposite materials; however, there is a lack of accurate material property characterization of individual CNCs. Here, a detailed study of the topography, elastic and adhesive properties of individual wood-derived CNCs is performed using atomic force microscopy (AFM). AFM experiments involving high-resolution dynamic mode imaging and jump-mode measurements were performed on individual CNCs under ambient conditions with 30% relative humidity (RH) and under a N_2 atmosphere with 0.1% RH. A procedure was also developed to calculate the CNC transverse elastic modulus (E_T) by comparing the experimental force−distance curves measured on the CNCs with 3D finite element calculations of tip indentation on the CNC. The E_T of an isolated CNC was estimated to be between 18 and 50 GPa at 0.1% RH; however, the associated crystallographic orientation of the CNC could not be determined. CNC properties were reasonably uniform along the entire CNC length, despite variations along the axis of 3−8 nm in CNC height. The range of RH used in this study was found to have a minimal effect on the CNC geometry, confirming the resistance of the cellulose crystals to water penetration. CNC flexibility was also investigated by using the AFM tip as a nanomanipulator.

1. Introduction

Cellulose is one of nature's wonders, the base reinforcement unit for the hierarchical structures used by various plant species giving them the unusual ability to provide high mechanical strength, a high strength-to-weight ratio, and high toughness. The impact on humankind is evident by the fact that natural cellulose-based materials (wood, hemp, cotton, and linen) have been used as engineering materials for thousands of years and continue today, as verified by the enormity of the worldwide industries in forest products, paper, textiles, and so forth. The more recent consumer push for products made from renewable and carbon neutral resources that are biodegradable with low environmental and animal/human health risks has revitalized research in cellulose-based composites. The goal is to produce cost-effective cellulose-reinforced composites that perform comparably to inorganic/mineral-based reinforced composites (e.g., glass fiber).[1−3] Additionally, advances in nanoscale science and engineering and characterization tools for use on cellulose present an opportunity for a new platform for research and technological innovations[4] in cellulose-based composites.

Cellulose is a linear chain of glucose molecules ($(C_6H_{10}O_5)_n$, n = 10 000−15 000) linked together through an acetal oxygen covalently bonding C1 of one glucose ring and C4 of the adjoining ring[3,5] (Figure 1a). Multiple cellulose chains hydrogen bond to each other to form elementary fibrils, which collect into microfibrils that are 5−50 nm in diameter and several micrometers in length and have regions that are disordered (amorphous-like) and highly ordered (crystalline)[2] (Figure 1b). These cellulose fibrils are the main reinforcement phase for the subsequent cellular structured plant tissues and can be extracted from plant cell walls by chemical−mechanical processes. Cellulose nanocrystals (CNCs) are obtained by the acid hydrolysis of cellulose under conditions where the amorphous regions are selectively hydrolyzed. For wood-based CNCs, the remaining crystalline regions are 3−10 nm in diameter and 100−300 nm long and retain the natural cellulose I crystalline structure.[6,7]

Cellulose nanocrystals have mechanical properties comparable to those of other reinforcement materials (Table 1): a high aspect ratio, low density (1.566 g/cm^3), and a reactive surface that facilitates grafting chemical species to achieve different surface properties (surface functionalization) and improved dispersion within a matrix polymer.[3,8] These features are favorable for the use of CNCs in composites. Favier et al.[9] completed the first study on CNC composites and observed that the addition of CNCs caused retention in the composite shear modulus at temperatures higher than the glass-transition temperature (T_g) of the matrix material. The observed reinforcing effect was attributed to the formation of a rigid CNC network governed by the percolation threshold and strong hydrogen bonding between CNCs. This mechanism was confirmed by Capadona et al.[10] while studying the reversible stiffness switching mechanism in the sea cucumber dermis. Active areas of CNC research include CNC processing,[3,6,7,11]

*Corresponding author. E-mail: rlahiji@purdue.edu; robertmoon@fs.fed.us.

(1) Bledzki, A.; Gassan, J. *Prog. Polym. Sci.* **1999**, *24*, 221−274.
(2) Eichhorn, S.; Baillie, C.; Zafeiropoulos, N.; Mwaikambo, L.; Ansell, M.; Dufresne, A.; Entwistle, K.; Herrera-Franco, P.; Escamilla, G.; Groom, L.; Hughes, M.; Hill, C.; Rials, T.; Wild, P. *J. Mater. Sci.* **2001**, *36*, 2107−2131.
(3) Samir, M. A. S. A.; Alloin, F.; Dufresne, A. *Biomacromolecules* **2005**, *6*, 612−626.
(4) Lucia, L.; Rojas, O. *Cellulose* **2007**, *14*, 539−542.
(5) O'Sullivan, A. C. *Cellulose* **1997**, *4*, 173−207.
(6) Araki, J.; Wada, M.; Kuga, S.; Okano, T. *Colloids Surf., A* **1998**, *142*, 75−82.
(7) Bondeson, D.; Mathew, A.; Oksman, K. *Cellulose* **2006**, *13*, 171−180.
(8) Orts, W. J.; Shey, J.; Imam, S. H.; Glenn, G. M.; Buttman, M. E.; Revol, J.-F. *J. Polym. Environ.* **2005**, *13*, 301−306.
(9) Favier, V.; Chanzy, H.; Cavaille, J. *Macromolecules* **1995**, *28*, 6365−6367.
(10) Capadona, J.; Shanmuganathan, K.; Tyler, D.; Rowan, S.; Weder, C. *Science* **2008**, *319*, 1370−1374.
(11) Dong, X.; Revol, J.-F.; Gray, D. *Cellulose* **1998**, *5*, 19−32.

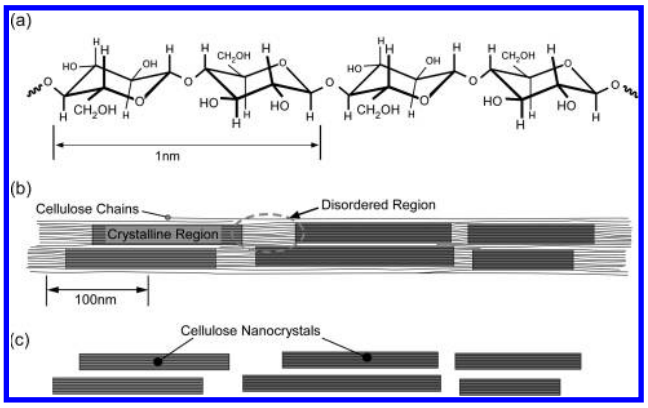

Figure 1. Schematics of (a) a single cellulose chain, (b) a cellulose microfibril showing ordered (crystalline) and disordered (amorphous) regions, and (c) cellulose nanocrystals after acid hydrolysis dissolved the disordered regions.

CNC self-assembly and chirality,[12−14] CNC thin film processing,[12,15] composite processing and CNC dispersion,[3,16] CNC surface functionalization,[16,17] CNC−matrix interphase[18] and composite properties, in particular, thermal stability,[16,19,20] mechanical strength,[8,21] stiffness,[8,17,19−21] elongation,[8,21] and composite swelling.[22]

The axial CNC properties have been considered to be of primary importance to CNC composite properties, but the load transfer through the CNC−matrix interphase dictates the composite mechanical properties[18,23] and the local changes in composition, structure, and bonding at the CNC−matrix interface alter the composite thermal properties.[18] To gain a better understanding of the role of CNCs in the resulting composite properties, it is imperative to characterize the transverse CNC properties and CNC surfaces. Unfortunately, there are limited characterization techniques available that can directly measure and quantify the transverse properties of individual nanoparticles[24] as well as surface chemistry. The purpose of this study is to address this gap by developing the necessary protocols for using atomic force microscopy (AFM) techniques to characterize CNC mechanical properties and surface characteristics. Additionally, the role of environmental change in the CNC properties is also investigated.

2. Background

In what follows, we outline the state of the art and the contributions of the present work with respect to (a) CNC elastic modulus estimates and (b) CNC surface chemistry measurement.

2.1. CNC Elastic Modulus Estimates. The crystal structures of cellulose polymorphs (I_α, I_β, II, III, IV) have been studied and debated extensively.[5] The five crystalline forms differ in terms of the geometry and orientation of the cellulose chains within their respective unit cells. The two main forms are cellulose I (natural or native) and cellulose II (regenerated, mercerization). Cellulose I is the polymorph discussed in this study because CNCs are produced from natural cellulose[32] and the acid hydrolysis of cellulose retains the cellulose I crystal structure within the CNCs.[6,7] There are two polymorphs that coexist in various proportions in cellulose I, a triclinic structure (I_α) and a monoclinic structure (I_β). There is limited consensus regarding the I_α/I_β ratio within natural cellulose, but in general, I_β is the dominate polymorph for higher-plant cell wall cellulose and tunicate,[33] whereas I_α is the dominate polymorph for bacteria[34] and algae.[35] It is unknown if the I_α/I_β ratio changes for CNCs as a result of their processing; however, I_α is the metastable form and can be converted to the more stable I_β,[34,35] thus it is likely that CNCs will retain a low I_α/I_β ratio. Also, the cross-sectional morphology of the CNCs is unknown, in which Figure 2 shows three possible cases.

The elastic properties of cellulose I crystalline regions have been investigated since the mid-1930s either by theoretical evaluations or by experimental measurements (wave propagation, X-ray diffraction, Raman spectroscopy, and AFM) and are summarized in Table 2. Theoretical evaluations have primarily investigated the role of cellulose crystal structure, the critical contribution of intramolecular and intermolecular hydrogen bonding,[39] and different theoretical approaches to modeling the elastic properties.[42] Most studies have focused on the elastic properties along the axial direction of the cellulose chain, and depending on the assumptions and boundary conditions used in the models, a range of elastic properties were obtained (Table 2). The elasticity perpendicular to the chain axis was considered by Tashiro and Kobayashi,[39] who reported a large amount of anisotropy in the cellulose I modulus, in which the axial modulus (parallel to the cellulose axis) was E_A = 167 GPa and the two transverse elastic moduli were E_{T1} = 11 GPa and E_{T2} = 50 GPa. The elastic

(12) Cranston, E.; Gray, D. *Biomacromolecules* **2006**, *7*, 2522−2530.
(13) Orts, W.; Godbout, L.; Marchessault, R.; Revol, J. *Macromolecules* **1998**, *31*, 5717−5725.
(14) Roman, M.; Gray, D. *Langmuir* **2005**, *21*, 5555−5561.
(15) Lefebvre, J.; Gray, D. *Cellulose* **2005**, *12*, 127−134.
(16) Petersson, L.; Kvien, I.; Oksman, K. *Comput. Sci. Technol.* **2007**, *67*, 2535−2544.
(17) Grunert, M.; Winter, W. T. *J. Polym. Environ.* **2002**, *10*, 27−30.
(18) Dufresne, A.; Kellerhals, M.; Witholt, B. *Macromolecules* **1999**, *32*, 7396−7401.
(19) Dubief, D.; Samain, E.; Dufresne, A. *Macromolecules* **1999**, *32*, 5765−5771.
(20) Noorani, S.; Simonsen, J.; Atre, S. *Cellulose* **2007**, *14*, 577−584.
(21) Samir, M.; Alloin, F.; M, M. P.; A, A. D. *Macromolecules* **2004**, *37*, 4313−4316.
(22) Sriupayo, J.; Supaphol, P.; Blackwell, J.; Rujiravanit, R. *Carbohydr. Polym.* **2005**, *62*, 130−136.
(23) Eitan, A.; Fisher, F. T.; Andrews, R.; Brinson, L. C.; Schadler, L. S. *Compos. Sci. Technol.* **2006**, *66*, 1162−1173.
(24) Tan, E.; Lim, C. *Compos. Sci. Technol.* **2006**, *66*, 1102−1111.
(25) Jr. Callister, W., In *Composites. Materials Science and Engineering: An Introduction*, 3rd ed.; John Wiley & Sons: New York, 1994.
(26) Kawabata, S.; Sera, M.; Kotani, T.; Katsuma, K.; Niwa, M.; Xiaoxin, C., Anisotropic Mechanical Properties of Advanced High Performance Fibers Obtained by a Single Fiber Testing System. *9th International Conference on Composite Materials* **1993**, 671−677.
(27) Hussain, F.; Hojjati, M.; Okamoto, M.; Gorga, R. E. *Compos. Mater.* **2006**, *40*, 1511−1575.
(28) Yu, M.-F.; Lourie, O.; Dyer, M.; Moloni, K.; Kelly, T.; Ruoff, R. *Science* **2000**, *287*, 637−640.
(29) Ding, S.-Y.; Himmel, M. E. *J. Agric. Food Chem.* **2006**, *54*, 597−606.
(30) Eichhorn, S.; Young, R. *Cellulose* **2001**, *8*, 197−207.
(31) Guhados, G.; Wan, W.; Hutter, J. *Langmuir* **2005**, *21*, 6642−6646.
(32) Beck-Candanedo, S.; Roman, M.; Gray, D. G. *Biomacromolecules* **2005**, *6*, 1048−1054.
(33) Belton, P.; Tanner, S.; Cartier, N.; Chanzy, H. *Macromolecules* **1989**, *22*, 1615−1617.
(34) Yamamoto, H.; Horii, F.; Hirai, A. *Cellulose* **1994**, *1*, 57−66.
(35) Yamamoto, H.; Horii, F. *Macromolecules* **1993**, *26*, 1313−1317.
(36) Jaswon, A.; Gillis, P. P.; Mark, R. E. Proceedings of the Royal Society of London. Series A, Mathematical and Physical Sciences, Vol. 306, No. 1486, (Sep. 10, 1968), pp 389−412.
(37) Tashiro, K.; Kobayashi, M. *Polym. Bull.* **1985**, *14*, 213−218.
(38) Kroon-Batenburg, L.; Kroon, J.; Northolt, M. *Polym. Commun.* **1986**, *27*, 290−292.
(39) Tashiro, K.; Kobayashi, M. *Polymer* **1991**, *32*, 1516−1526.
(40) Marhofer, R.; Reiling, S.; Brickmann, J. *Ber. Bunsen-Ges.* **1996**, *100*, 1350−1354.
(41) Sturcova, A.; Davies, G. R.; Eichhorn, S. J. *Biomacromolecules* **2005**, *6*, 1055−1061.
(42) Tanaka, F.; Iwata, T. *Cellulose* **2006**, *13*, 509−517.
(43) Meyer, K.; Lotmar, W. *Helv. Chim. Acta* **1936**, *19*, 68−86.
(44) Sakurada, I.; Nukushina, Y.; Ito, T. *J. Polym. Sci.* **1962**, *57*, 651−660.
(45) Sakurada, I.; Ito, T.; Nakamae, K. *Makromol. Chem.* **1964**, *75*, 1−10.
(46) Matsuo, M.; Sawatari, C.; Iwai, Y.; Ozaki, F. *Macromolecules* **1990**, *23*, 3266−3275.
(47) Nishino, T.; Takano, K.; Nakamae, K. *Polym. Sci.* **1995**, *33*, 1647−1651.
(48) Iwamoto, S.; Kai, W.; Isogai, A.; Iwata, T. *Biomacromolecules* **2009**, *10*, 2571−2576.

Table 1. Properties of Several Reinforcement Materials[a,b,c]

material	density (g/cm^3)	elastic modulus (GPa) E_A	elastic modulus (GPa) E_T	tensile strength (GPa)	reference
fibers					
E-glass	2.5	72	−	3.5	25
Kevlar-49	1.4	124	−	3.5	25
	−	130	2.5	−	26
carbon	1.8	150−500	−	1.5−5.5	25
high carbon steel wire	7.8	210	−	4.1	25
whiskers					
graphite	2.2	690	−	20	25
aluminum oxide	3.9	415−550	−	14−28	25
nanoparticles					
clay platelets	−	170	−	−	27
MWCNTs[d]	−	270−950	−	11−63	28
boron whiskers	−	250−360	−	2−8	29
graphite platelets	−	1000	−	−	27
cellulose					
microfibrils	−	25 ± 4	−	−	30
	−	78 ± 17	−	−	31
nanocrystals (CNC)	1.5	110−200	11−57	−	see Table 2

[a] E_A is the elastic modulus in the axial direction. [b] E_T is the elastic modulus in the transverse direction. [c] Symbol − indicates a lack of information on the subject. [d] MWCNTs are multiwalled carbon nanotubes.

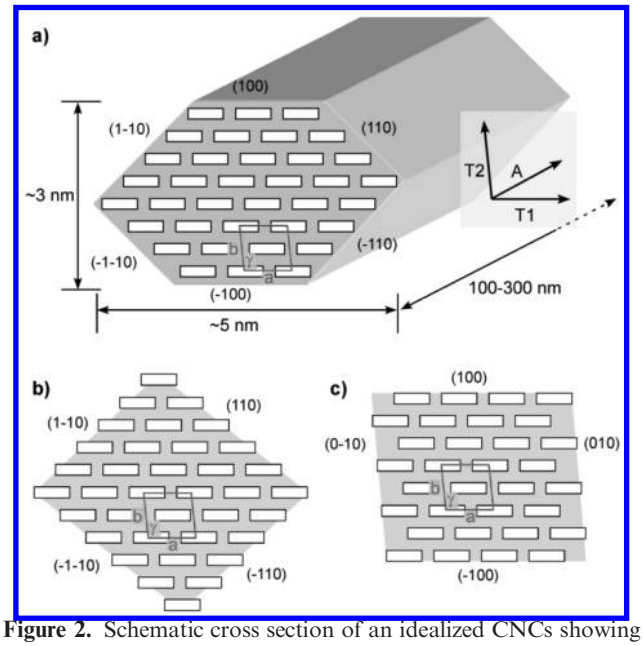

Figure 2. Schematic cross section of an idealized CNCs showing the monoclinic arrangement of 36 cellulose chains (cellulose I_β crystalline structure). The box indicates the cellulose I_β lattice with $a = 0.786$ nm, $b = 0.817$, and $\gamma = 97°$.[5] (a) shows the cross section as described by Ding and Himmel.[29] (b, c) Other possible cross sections. The anisotropic structures of cellulose I in the axial and transverse directions are labeled A, T1, and T2, respectively (consistent with Table 2).

modulus anisotropy is associated with the anisotropy in the cellulose chain arrangement within the CNC in the three principle directions (Figure 2). Note that throughout the article the following terminology is used for the elastic modulus along the CNC axial direction (E_A) and the CNC transverse direction (E_T).

The elastic properties of cellulose I have been experimentally measured only in the axial direction using bulk-sized specimens with the cellulose microfibrils preferentially aligned in the loading direction, where small axial strains in the crystalline cellulose structure were used to calculate E_A (Table 2). For CNCs, only E_A has been experimentally measured. Šturcová et al.[41] calculated E_A = 143 GPa based on the shift in the characteristic Raman spectroscopy peak for cellulose I (1095 cm^{-1}) of the tunicate CNC-epoxy composite subjected to three-point bending. Additionally, Iwamoto et al.[48] calculated a range of E_A = 110−200 GPa using AFM three-point bending of tunicate CNCs. The AFM tip was used as the third loading point and measured the applied force and the displacement of CNCs that bridged nanoscale grooves fabricated on the substrate. To date, there has been no reported experimental measurements of CNC E_T.

This current study addresses the gap in the literature of transverse elastic property measurements of individual CNCs. AFM techniques were used to measure the transverse stiffness along the length of CNCs. Several locations along the CNC length were measured, which provided the opportunity to assess the uniformity of the transverse stiffness along the CNC crystal. Additionally, the CNCs were exposed to 30 and 0.1% relative humidity (RH), and the influence of RH on the measured transverse stiffness was investigated. Finally, the transverse stiffness measurements were used to calculate the CNC E_T.

2.2. CNC Surface Chemistry Measurement. The CNC−matrix interface strongly influences composite properties. To gain insight into the mechanisms controlling this interface, it is first necessary to characterize the starting and modified CNC surfaces quantitatively in terms of exposed functional groups and the uniformity of coverage prior to their incorporation in a polymer matrix. A literature review by Gardner et al.[49] summarizes the surface chemistry measurements of cellulose-based materials including thin films, fibers, microcrystalline cellulose, and CNCs.

In situ surface characterization offers the additional capability of monitoring changes in the CNC surface chemistry as a direct result of changes in the environment. Surface chemistry and functionalization have been investigated for microcrystalline cellulose[50] and cellulose fibers using imaging techniques that employ the labeling of target molecules that then chemically bond to specific sites on a given surface. Labeling by organic dyes, semiconductor quantum dots, and fluorescent proteins has been used, and these have been imaged using fluorescence spectroscopy, AFM, and transmission electron microscopy. These techniques provide a visual map of the surface chemistry and qualitative concentrations.

(49) Gardner, D. J.; Oporto, G. S.; Mills, R.; Samir, M. A. S. A. *J. Adhes. Sci. Technol.* **2008**, *22*, 545−567.
(50) Xu, Q.; Tucker, M. P.; Arenkiel, P.; Ai, X.; Rumbles, G.; Sugiyama, J.; Himmel, M. E.; Ding, S.-Y. *Cellulose* **2009**, *16*, 19−26.

Table 2. Literature Summary of Cellulose I Elastic Modulus Measurements and Modeling[a]

reference	material	elastic modulus (GPa) E_A	E_{T1}	E_{T2}	method
cellulose I Modeling	−				
36	−	76	51	57	w/H bonding
37	−	173	−	−	w/H bonding
38	−	136 ± 6	−	−	w/H bonding
39	−	167	11	50	w/H bonding
40	−	128	−	−	w/H bonding
41	−	145	−	−	w/H bonding
42	−	124−155	−	−	w/H bonding
cellulose I Experimental					
43	ramine	90	−	−	wave propagation
	flax	78−108	−	−	wave propagation
44	ramine	137	−	−	X-ray diffraction
45	ramine	130	−	−	X-ray diffraction
46	ramine	120−135	−	−	X-ray diffraction
47	ramine	138	−	−	X-ray diffraction
cellulose Nanocrystals					
41	tunicate	143	−	−	Raman
48	tunicate	110−200	−	−	AFM

[a] Symbol − indicates a lack of information on the subject.

Unfortunately, there are a limited number of characterization techniques that have been applied to CNCs because of their small size and the additional constraints that this places on useful imaging methods. CNC morphology has been studied using electron microscopy techniques and AFM techniques. Near-atomic-resolution AFM topography imaging has claimed to resolve cellulose surface crystalline structure[51] in which different features on the CNC surface were assigned to the repeating functional groups of the cellulose crystalline structure (i.e., glucose rings, hydroxyl groups, etc). To our knowledge, no studies have investigated the surface chemistry of individual CNCs and how they change as a function of the testing environment.

This current study addresses a gap in the literature by assessing the uniformity of CNC surface chemistry along its length and the in situ changes in CNC surface chemistry as a result of changing environmental conditions. The force required to remove the AFM tip from contact with the CNC surface, "adhesion", was used to assess the tip−surface interaction, providing a qualitative measure of the CNC surface chemistry. Because the technique measures several locations along the CNC length, the uniformity of the tip−surface interaction along the CNC crystal was assessed.

3. Experimental Procedure

3.1. CNC Processing and Sample Preparation. The CNC preparation procedure follows those described by Beck-Candanedo et al.[32] Acid hydrolysis was completed using an 8 to 1 weight ratio of 64% sulfuric acid to commercial-grade dissolving pulp at 45 °C for 1 h. This mixture was then diluted with deionized water to quench the reaction, centrifuged, washed, underwent dialysis for about a week to remove any remaining acid, and was ultrasonicated to provide mechanical agitation to disperse the cellulose crystals. A final centrifuge separation step is used to remove the larger agglomerates in the CNC suspension.

The samples used for AFM imaging were produced by placing a few drops of CNC solution (∼1.2 wt % suspension) onto a 1 cm × 1 cm square of freshly cleaved mica. Before these drops dried, the mica surface was rinsed with deionized water and blown dry with N_2 gas. This method resulted in well-dispersed CNCs that were strongly adhered to the mica substrate. The rinsing and N_2 blow drying steps were implemented for two reasons: first, to lower the concentration of CNCs on the mica surface; second, the remaining CNCs would be the ones that were well adhered to the mica surface.

3.2. AFM Measurements. A Nanotec Electronica scanning probe instrument (Madrid, Spain) mounted in an environmental chamber was used in this study for AFM imaging. The atmosphere could be set to either ambient conditions having ∼30% relative humidity (RH) or to ∼0.1% RH by flowing N_2 gas from liquid nitrogen boil off into the chamber. WSxM software (version 12.0) was used to process the AFM images.[52] Aluminum-coated silicon cantilevers (Asylum AC240TS, Santa Barbara, CA) having a nominal tip radius of < 10 nm, a nominal spring constant of 2 N/m, and a nominal resonance frequency of 70 kHz were used in this study. For each cantilever, the spring constant was calibrated using Sader's method.[53] Several AFM modes were used in this study: dynamic (noncontact)-mode AFM for topography measurements, jump-mode AFM[54] for stiffness and adhesion measurements, and contact-mode AFM for CNC manipulation experiments.

Amplitude-modulated AFM (AM-AFM)[55,56] was used for topography imaging. An amplitude set point of 90% of A_o was used, where A_o is the free cantilever amplitude of ∼80 nm. A topography AFM image of a typical CNC on a mica substrate is shown in Figure 3. At this set-point amplitude, the cantilever oscillated in the attractive regime.[57] AFM tip convolution effects[58] artificially increase the CNC in-plane width. However, the CNC height can be determined unambiguously from the height of the crystal surface above the mica surface. For axisymmetric objects (a reasonable description of the morphology of CNCs derived from wood), this height can be used to estimate the object width. The CNC shown in Figure 3 is 220 nm in length, and its height varies from 5 to 7 nm (Figure 3c) along the line drawn in Figure 3a. Typically, the CNCs produced for this study were 100−300 nm in length and 2−8 nm in height. Additionally, the height along a given CNC length was not constant, typically undergoing a 2−4 nm change in height. This is consistent with that observed in other studies.[3,6,7,11]

(51) Baker, A. A.; Helbert, W.; Sugiyama, J.; Miles, M. J. *Biophys. J.* **2000**, *79*, 1139−1145.

(52) Horcas, I.; Fernandez, R.; Gomez-Rodriguez, J. M.; Colchero, J.; Gomez-Herrero, J.; Baro, A. M. *Rev. Sci. Instrum.* **2007**, *78*, 013705

(53) Sader, J. E.; Larson, I.; Mulvaney, P.; White, L. R. *Rev. Sci. Instrum.* **1995**, *66*, 3789−3798.

(54) Pablo, P. J. d.; Gomez-Herrero, J.; Baro, A. M. *Appl. Phys. Lett.* **1998**, *73*, 3300.

(55) García, R.; Pérez, R. *Surf. Sci. Rep.* **2002**, *47*, 197−301.

(56) Raman, A.; Melcher, J.; Tung, R. *Nano Today* **2008**, *3* 20−27.

(57) Anczykowski, B.; Krüger, D.; Fuchs, H. *Phys. Rev. B* **1996**, *53* 15485.

(58) Yang, D.-Q.; Xiong, Y.-Q.; Guo, Y.; Da, D.-A.; Lu, W.-G. *J. Mater. Sci.* **2001**, *36*, 263−267.

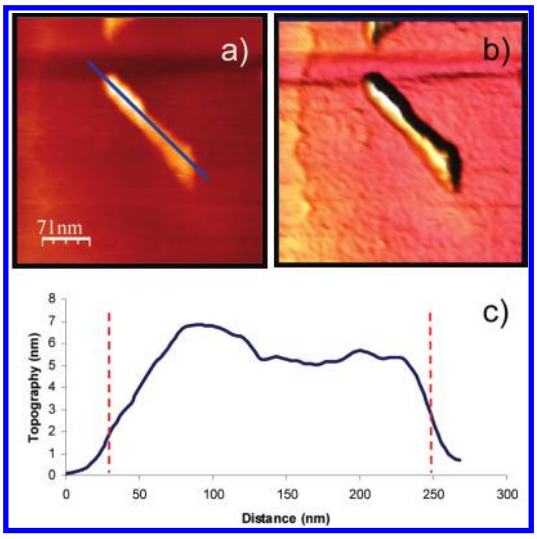

Figure 3. (a) A 2D dynamic-mode AM-AFM image of a wood-based CNC on a mica substrate having a length of 220 nm. (b) A 3D image of the CNC shown in image a. (c) The height profile of the line along the length of the CNC in part a is plotted and shows the CNC to have a length of 220 nm, with its height varying along the length from 5 to 7 nm.

Jump-mode AFM[54] was used to measure the stiffness and adhesion between the AFM tip and the contacting surface. WSxM's general spectroscopy imaging (GSI) mode was used to acquire the force (F) versus z-displacement distance of the piezo, $F(z)$ curves. This z displacement is the sum of the cantilever bending (x) and sample indentation (δ). The $F(z)$ data was acquired at every imaging point from which the effective stiffness and adhesion as a function of position across an image could be inferred. The effective stiffness, k_{eff}, of the AFM contact is composed of two contributions in series: the cantilever stiffness, k_c, and the tip−sample contact stiffness, k_{sample}. k_c is obtained by Sader's method, and $k_{\text{sample}} = dF/d\delta$. The slope of the $F(z)$ data after the AFM tip contacts the sample surface is used to calculate the k_{eff} (i.e., dF/dz), and the adhesion was estimated from the discontinuity in the $F(z)$ data during AFM tip withdrawal from the surface. The protocols for such an analysis are well established and are described in detail elsewhere.[59] The effective stiffness and adhesion measurements from the $F(z)$ data were used to assess the uniformity of the CNC elastic response and surface chemistry. The effective stiffness measurements were further used to calculate the E_T of CNCs.

The influence of changing RH on CNC topography, adhesion, and stiffness was investigated in situ on the same CNC. This was completed by initially locating an isolated CNC on the mica surface by scanning in dynamic mode AM-AFM. The chamber was then filled with dry N_2 gas, the sample was held in this environment for >20 min, and $F(z)$ data was measured in jump-mode AFM. The chamber was then exposed to ambient conditions, the sample was held in this new environment for >20 min, and $F(z)$ data was remeasured on the same CNC. An RH detector (Mannix, DL 8829) was located ∼5 cm from the AFM tip location, providing an RH measure within the vicinity of the AFM measurements.

3.3. AFM Manipulation of CNCs. To investigate CNC flexibility, contact-mode AFM was used to manipulate CNCs under ambient conditions. This was completed by initially imaging in dynamic-mode AFM and locating isolated CNC on the mica surface. Then in contact-mode AFM the lithographic capability of the WSxM software[52] was used to precisely control the normal force between the AFM tip and the substrate as well as the path of the AFM tip so that the tip pushed against a given CNC.

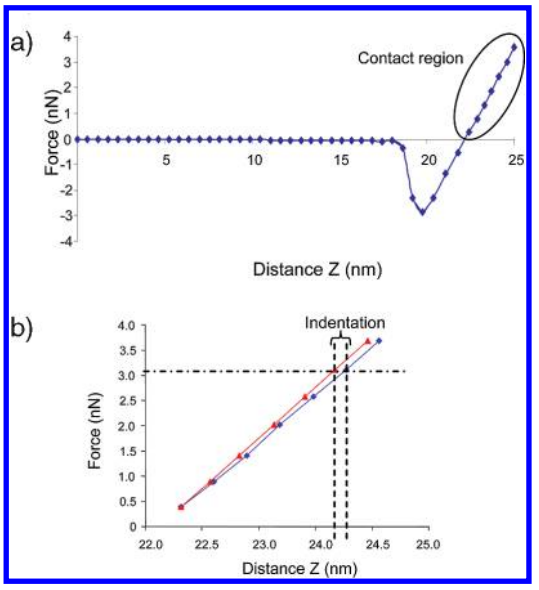

Figure 4. (a) Plot of $F(z)$ data acquired on a CNC. (b) The area marked by an oval is shown with the measured $F(z)$ curve (blue ♦) on CNC and on mica (red ▲). By finding the difference between z values at a given force, the CNC indentation can be obtained at each force value, $F(\delta)$.

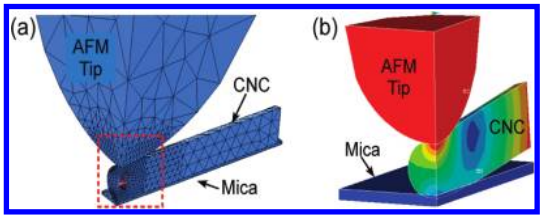

Figure 5. Three-dimensional quarter-symmetry model of the CNC-AFM indentation. (a) ∼20 000 elements and the mesh is refined where the contact or large deformation happens. The dashed square represents the enlarged area shown in part b. (b) Stress profile within the CNC during loading.

Subsequent dynamic-mode AM-AFM images were used to determine if the individual CNC moved (i.e., rolling or sliding along the surface) or was permanently deformed (bending) or fractured.

3.4. CNC Transverse Elastic Modulus Calculations. To extract E_T from the AFM-measured $F(z)$ curves on CNCs, this data needs to be converted into a force−indentation $F(\delta)$ curve.[60] This is a standard process in elastic property extraction in AFM and is accomplished by comparing the measured $F(z)$ data for the feature of interest (CNCs in this case), with that for a hypothetically infinitely stiff substrate, mica in this case. At any applied force value, the corresponding difference in z-distance between the $F(z)$ curves provides a measure of the CNC indentation at that force value[60] (Figure 4). The resulting $F(\delta)$ curve can be fitted to physics-based models that predict the AFM tip−substrate contact mechanics, and the elastic modulus can be estimated by tuning the theoretical elastic modulus value to match the theoretical prediction with observed data. In the current study, finite element analysis was used.

A 3D quarter-symmetry model was created with the ANSYS finite element package (ANSYS Inc., Houston, TX). The CNC is modeled as a solid cylinder with a diameter of 6 nm, the AFM tip is modeled as a rigid sphere with a radius of 20 nm, and the supporting substrate is modeled as a rigid brick having the properties of mica, shown in Figure 5. To account for the tip

(59) Schaefer, D. M.; Gomez, J. *J. Adhes.* **2000**, *74* 341− 359.

(60) Butt, H.-J.; Cappella, B.; Kappl, M. *Surf. Sci. Rep.* **2005**, *59*, 1−152.

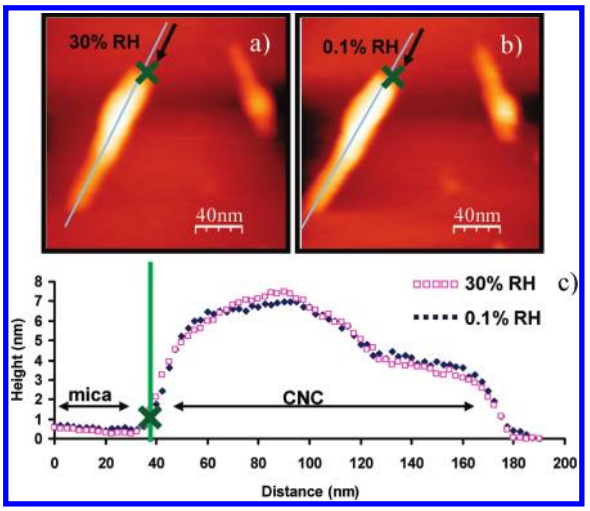

Figure 6. Topography images obtained in GSI mode data at (a) 30% RH and (b) 0.1% RH. Height profiles of (pink □) 30% RH and (blue ♦) 0.1% RH given in part c are along the lines drawn in parts a and b, respectively.

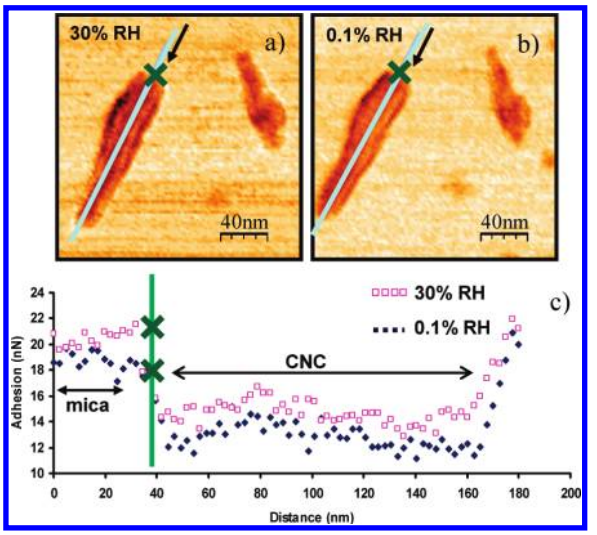

Figure 7. Adhesion images obtained in GSI mode data at (a) 30% RH and (b) 0.1% RH. The adhesion profiles of (pink □) 30% RH and (blue ♦) 0.1% RH given in part c are along the lines drawn in parts a and b, respectively.

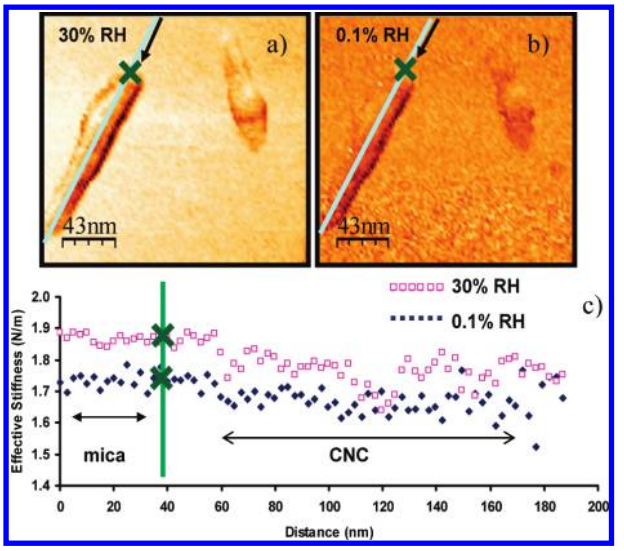

Figure 8. Effective stiffness images obtained in GSI mode data at (a) 30% RH and (b) 0.1% RH. The effective stiffness profiles of (pink □) 30% RH and (blue ♦) 0.1% RH given in part c are along the lines drawn in parts a and b, respectively.

blunting that occurs during jump-mode testing, the modeled AFM tip radius is larger than the nominal tip radius of 10 nm quoted by the AFM manufacturer. Note that because the modeled CNC has such a small radius the theoretical $F(z)$ curves were found not to be a strong function of the AFM tip radius.

The CNC-AFM contact model contained ~20 000 elements, and the mesh is refined where the contact or large deformation was localized. A systematic grid and domain convergence study was performed. Two contact pairs, one between the probe and the upper surface of the CNC cylinder and the other between the lower surface of the CNC and the upper surface of the supporting surface, were defined. To obtain a stable solution, vertical displacements were applied to the probe, and the other two degrees of freedom (DOFs) of the tip and all DOFs of the supporting surface were fixed. The vertical displacement was increased gradually, and the corresponding contact forces on the probe−CNC contact pair were calculated. In this way, the model predicted the force versus indentation depth $F(\delta)$ curve. By adjusting the CNC's E_T in the ANSYS model, it was possible to match the theoretical $F(\delta)$ curve to the experimental $F(\delta)$ curve. The best fit between experimental and model predictions was completed by using a function $f(E)\delta n$, where δ is the indentation fitted to the experimental data and n was obtained from the average of theoretical $F(\delta)$ curves, which was 1.534. The E_T that resulted in the best fit was used to estimate E_T for the CNC.

To minimize errors when comparing the experimental versus ANSYS model $F(\delta)$, the contact geometry between the AFM tip and the CNC should be similar and preferably be more like the idealized contact geometry used in the ANSYS model. The idealized contact geometry was considered to be along the center of the CNC. Experimentally, this was completed by selecting only the $F(z)$ curves that were measured along the center of the CNC. One main advantage of the jump-mode AFM measurements performed in this study is that $F(z)$ curves are measured from every imaging point, so it was relatively simple to select $F(z)$ curves that were along the center of the CNC.

4. Results and Discussion

4.1. Jump-Mode AFM. Over a dozen different CNCs have been imaged with jump-mode AFM, and values for topography, adhesion, and the effective stiffness all follow the same trends. For a typical CNC, the jump-mode AFM topography, adhesion, and effective stiffness measurements are summarized in Figures 6, 7, and 8, respectively. Part a is the measurement map at 30% RH, and part b is at 0.1% RH. Part c is the measurement profile along the CNC length, which was taken at the center of the CNC to minimize AFM tip-edge artifacts that are well known in SPM imaging. Parts a and b show the location of the line profile along the CNC, and the black arrow indicates the direction of the drawn line profile. For the measurements shown in Figure 6, 7, and 8, the cantilever spring constant was 2.1 N/m. The topography profile (Figure 6c) shows that the length of the CNC is ~140 nm and its height varies from 3 to 8 nm above the mica substrate. The CNC height measurement was consistent for the two different RHs in which the small changes were within the ±1 nm run-to-run variation in AFM height measurement. It is unlikely that CNCs would swell with increasing RH, which would be associated with water molecules penetrating the CNC and diffusing between and causing the separation of the cellulose chains. This is confirmed in the study by Sakurada et al.,[44] who showed that changes in humidity did not alter the cellulose I lattice spacing as measured by X-ray diffraction.

The analysis of the adhesion and stiffness was taken from the data lying in the 50−150 nm range, in which there were ∼40 individual measurements completed along this length corresponding to 4 measurements per 10 nm of CNC, demonstrating the high spacial resolution of this technique. In what follows are the first approximations in the analysis of the contrast in adhesion and effective stiffness for the measurements completed on mica versus CNCs.

It should be noted that it is difficult to compare the actual values of adhesion and effective stiffness of different CNCs. One reason for this is related to the changes in AFM tip geometry that occur because of tip fouling as the ∼10 nm tip repeatedly comes into contact with the substrate throughout scanning in jump-mode AFM. Because of this, the tip−substrate contact geometry changes, which then alters the measured $F(z)$ curves and alters the calculations for both the adhesion and effective stiffness.[60] Likewise, the AFM cantilevers are typically replaced after only a few measurements, thus there will be a different AFM tip shape, radius, and cantilever stiffness.

4.1.1. Adhesion Measurements. The adhesion measurements (Figure 7) show that the AFM tip pull-off forces on the CNC are lower than on mica. At 0.1% RH, the average adhesion (pull-off force) on mica is 18.9 ± 0.5 nN and that on the CNC is 13.0 ± 0.9 nN. Likewise, at 30% RH the average adhesion (pull-off force) on mica is 20.2 ± 0.5 nN, and on the CNC it is 14.7 ± 0.9 nN. The larger adhesion for the 30% RH testing environment is associated with water adsorption on the surface increasing the water meniscus formation between the AFM tip and the contacting surface.[60]

The adhesion contrast between mica and CNC can come about by three mechanisms: meniscus effects caused by moisture condensing in the tip-contact region, contact geometry effects, and surface energy effects. By considering the 0.1% RH case and that both mica and CNCs are hydrophilic, the influence of meniscus effects can be considered to be minimal.[46] Contact geometry effects can be considered by using the Johnson−Kendall−Roberts (JKR) model to predict the separation of two spheres,[61] which occurs at

$$P_{ij} = 3W_{ij}\pi\frac{R_iR_j}{(R_i + R_j)} \quad (1)$$

where P_{ij} is the force required to separate surfaces i and j, W_{ij} is the change in energy when separating surface i from surface j, and R_i and R_j are the radii of curvature of surfaces i and j, respectively. The contact geometry effect can be estimated through comparison between the AFM tip in contact with the flat mica surface versus contact with a mica surface having a nanobump that simulates a CNC. For this case, 1 denotes the AFM tip surface (having a radius of R_1 = 10 nm), 2 denotes the flat mica surface (having a radius of R_2 = ∞), and 3 denotes a hemispherical nanobump on the mica surface (having a radius of R_3 = 3.5 nm). Because R_2 is much greater than R_1 and R_3, the ratio of P_{12} to P_{13} would be

$$\frac{P_{12}}{P_{13}} \cong \frac{W_{12}}{W_{13}}\left(1 + \frac{R_1}{R_3}\right) \quad (2)$$

For the case when the nanobump on the mica surface is composed of mica, then $W_{12} = W_{13}$, and when substituting in for R_1 and R_3, the resulting P_{12}/P_{13} ratio is ∼3.85. This suggests that differences in the contact geometry will have a large effect on the measured adhesive force; in particular, the adhesive force for the AFM tip in contact with mica should be nearly 4 times greater on a flat surface than that on a hemispherical nanobump of comparable radius of the CNC. Thus, it should be expected that the adhesion measurements are lower for CNC verses mica solely on the basis of differences in tip−surface contact geometry. This approach is only a general approximation; there will be some error (based on differences in contact shape) when applying the hemispherically shaped mica nanobump results to the rod-shaped CNC.

To assess surface energy effects, we now consider the case in which $W_{12} \neq W_{13}$. A similar comparison to that above can be made using eq 2, with the same values for R_1 and R_3 but the experimentally measured average adhesive forces substituted in for P_{12} and P_{13}, which for the 0.1% RH condition are ∼19 and ∼13 nN, respectively. Using this relationship, the resulting AFM-tip CNC contact surface energy was found to be ∼2.5 times larger than AFM-tip mica surface energy. Interestingly, even though the measured adhesive force is lower for the CNC than for mica, by accounting for differences in contact geometry (i.e., the larger AFM-tip mica contact area) it has been shown that the contacting surface energy is actually greater for CNCs than for mica.

4.1.2. Effective Stiffness Measurements. The effective stiffness measurements (Figure 8) for the CNC are slightly lower than for the mica. At 0.1% RH, the average effective stiffness on mica is 1.74 ± 0.02 N/m and that on CNC is 1.67 ± 0.04 N/m. Likewise, at 30% RH the average effective stiffness on mica is 1.85 ± 0.03 N/m and that on CNC is 1.77 ± 0.05 N/m. The larger effective stiffness for the 30% RH testing environment is associated with water meniscus effects.[60] Note that the effective stiffness on the CNC is not very different from that on mica. This is to be expected because CNC and mica are not soft materials, so k_{sample} for mica is essentially infinite and on CNC $k_{sample} \gg k_c$. In this case, k_{eff} will change very little between mica and CNC. When taking averages, though, over this data set and over measurements on other CNCs (multiple), we have measured higher stiffness with the AFM tip in contact with the mica than with CNC.

The effective stiffness contrast between mica and CNC can come about by three mechanisms: meniscus effects caused by moisture condensing in the tip-contact region, contact geometry effects, and material property effects. By considering the 0.1% RH case, the influence of meniscus effects can be considered to be minimal.[46] Geometry effects on the contact stiffness can be estimated by using Hertz's contact mechanics[62]

$$k_{ij} = (6PE_{ij}^2)^{2/3}\left(\frac{R_i + R_j}{R_iR_j}\right)^{1/3} \quad (3)$$

where k_{ij} is the contact stiffness for contact surfaces i and j, P is the applied load, E_{ij} is the effective contact modulus for both contacting bodies i and j in series, and R_i and R_j are the radii of curvature of surfaces i and j, respectively. The contact geometry effect can be estimated through a comparison between the AFM tip in contact with the flat mica surface versus contact with a mica surface having a nanobump that simulates a CNC. For this case, 1 denotes the AFM tip surface (having a radius of R_1 = 10 nm), 2 denotes the flat mica surface (having a radius of R_2 = ∞), and 3 denotes a hemispherical nanobump on the mica surface (having

(61) Johnson, K.; Kendal., K. *Proc. R. Soc. London* **1971**, *324*, 301−313.

(62) Johnson, K. L. *Contact Mechanics*; Cambridge University Press: Cambridge, England, 1985.

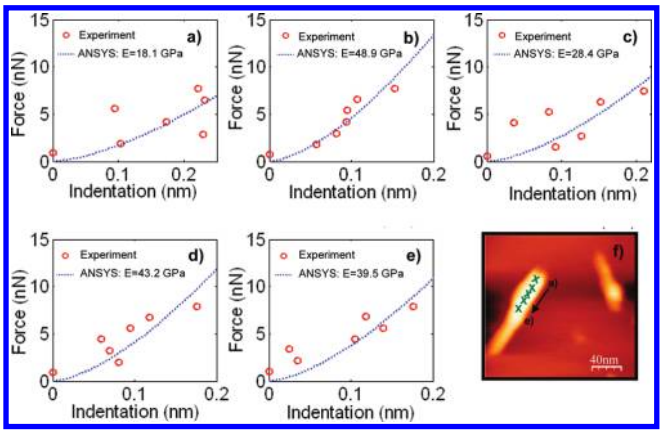

Figure 9. (a−e) Force−indentation plots of CNC in nitrogen gas (0.1% RH) with ANSYS simulation results overlaid and the resulting estimated E_T. (f) Crosses show the location of each force−indentation on the CNC.

a radius of $R_3 = 3.5$ nm). Because R_2 is much greater than R_1 and R_3, the ratio of k_{12} to k_{13} would be

$$\frac{k_{12}}{k_{13}} \cong \left(\frac{E_{12}}{E_{13}}\right)^{2/3} \left(\frac{R_1 R_3}{R_1 + R_3}\right)^{1/3} \quad (4)$$

For the case when the nanobump on the mica surface is composed of mica, then $E_{12} = E_{13}$, and when substituting in for R_1 and R_3, the resulting k_{12}/k_{13} ratio is ~1.4. This suggests that the resulting effective stiffness for the AFM tip in contact with mica should be ~1.4 times greater than the effective stiffness for that on the nanobump of comparable radius of the CNC. Thus, it should be expected that the effective stiffness measurements are lower for CNC verses mica, solely on the basis of differences in tip−surface contact geometry. This approach is only a general approximation; there will be some error when relating the results of the hemispherically shaped mica to the rod-shaped CNC because of differences in the AFM tip−CNC contact shape and the second contact region between CNC and mica, which was not accounted for. With this in mind, because the small difference in the experimentally measured effective stiffness between mica and CNC is lower than 1.4, this suggests that CNC has a stiffness that is similar to or greater than mica.

Note that the finite elemental model used to extract the elastic modulus from the effective stiffness results considers a spherical-rod contact geometry that more accurately simulates the AFM tip−CNC contact and also includes contributions from the CNC−mica contact (Figure 5a).

4.2. CNC Transverse Elastic Modulus. The E_T calculations were completed at five locations along the same CNC used in the stiffness and adhesion measurements. To minimize the potential water meniscus effect on the calculations, the CNC E_T calculations were completed only for data collected under the 0.1% RH condition. Figure 9 shows the five sets of $F(\delta)$ data (Figure 9a−e) obtained from $F(z)$ data at the locations shown with crosses in Figure 9f. The best fit between the ANSYS model and the experimental data occurs for $E_T = 18.1$, 48.9, 28.4, 43.2, and 39.5 GPa.

The wide variation in the extracted E_T arises from several aleatory uncertainties: (a) Indentation uncertainty: the first and foremost is the large uncertainty in the indentation measurement because the measured $F(z)$ curves on mica and CNC differ slightly and the indentation is the difference between the two curves that differ slightly. (b) Indentation location uncertainty: the AFM indentation does not occur exactly at the highest point on the CNC cross section; there is small aleatory uncertainty connected with the location of the indentation, which in turn influences the force required to make a certain indentation. (c) Tip radius and roughness uncertainty: between one indentation and another, the tip roughness can change slightly because of inelastic tip−sample interactions such as the plastic deformation of tip asperities, tip fouling, and so forth. The presence of asperities on the tip can significantly influence the force curve because the effective radius that indents the sample changes with changing roughness. By keeping the forces low (less than 8 nN), we minimize the possibility of tip damage/change but the mechanism does exist nevertheless and leads to uncertainty in the measured forces. As a consequence of these aleatory uncertainties, there is scatter primarily along the indentation axis and secondarily along the force axis (Figure 9a−e). The observed variability in the elastic modulus can be directly attributed to these measurement uncertainties because they prevent good fits of the finite element models with the measured data. The problem also comes with its epistemic uncertainties because a finite element model is being used to back out the elastic modulus. Epistemic or modeling uncertainty will lead to an offset in the elastic modulus prediction, not to the observed scatter.

The range of $E_T = 18-50$ GPa in nitrogen measured in the current study is similar to that predicted by the modeling studies of Tashiro and Kobayashi[39] ($E_{T1} = 11$ GPa and $E_{T2} = 50$ GPa) and Jawson[36] ($E_{T1} = 51$ GPa and $E_{T2} = 57$ GPa) for the two principal crystallographic orientations in the transverse section (Figure 2). Unfortunately, relating the E_T measured in the current study to a specific crystallographic orientation is challenging because it is difficult to estimate the crystallographic orientation of CNC deposited on mica. This is also challenging because it is dependent on the shape of the CNC after acid hydrolysis and the crystallographic planes that are exposed at the CNC surface, both of which are not well understood or characterized. In spite of our inability to distinguish between the E_T along the two different transverse directions, one clear implication of this work is that it confirms experimentally that the E_T values of CNCs are about an order of magnitude lower than the E_A values.[36,39]

4.3. CNC Manipulation. The deformation of individual CNCs is crucial to their mechanical role within CNC composites and filters. The AFM nanomanipulation provides a unique technique by which to explore the influence of an applied bending force on the CNC deformation, providing insight into the strength and flexibility of CNCs. CNCs were manipulated in contact-mode AFM by pushing an AFM tip against a given CNC. Figure 10 shows dynamic-mode AFM topography images of two CNCs prior to and after manipulation (crystals A and B). The white arrows indicate the tip path used to execute the CNC manipulations. Tip normal forces in the range of 3−5 nN were insufficient to cause the relative motion of the CNCs after the tip encountered them. By increasing the normal force into the 8−10 nN range, it was observed empirically that crystals A and B could be bent. The small radius of the bending curvature (i.e., large amount of bending over an ~100 nm crystal length) with no apparent fracturing is surprising because it is believed that the stiffening contribution of interhydrogen bonding between neighboring cellulose chains within the crystalline cellulose will resist local cellulose chain deformation resulting from an applied load.

There is some aggregation of crystals in this sample, thus an alternative explanation for the bending cannot be ruled out. It is possible that crystals A and B are actually aggregates of multiple smaller CNCs and that the bending of crystals A and B are actually a result of two or more CNCs sliding relative to each other. With the likelihood of structural defects and lower

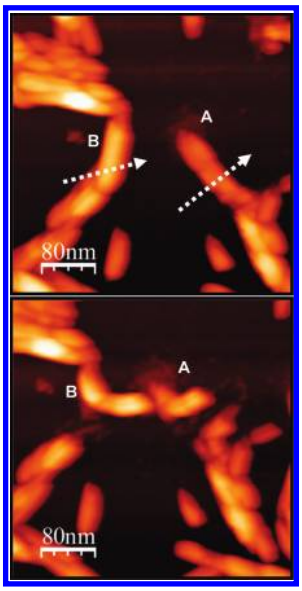

Figure 10. Topography images of AFM nanomanipulation of two CNCs (labeled A and B) showing how the applied lateral force apparently bends the initially straight CNCs. Arrows indicate the direction of tip movement for nanomanipulation.

hydrogen bonding across the CNC−CNC interface within the agglomerates, it is considered that the bonding strength between the CNCs is lower than that of the idealized cellulose I_β crystal structure making up the CNCs, Thus, if one considers the weak-link analogy, then deformation would occur at the interface between the CNC agglomerates.

5. Conclusions

This work has focused on the mechanical property characterization of wood-derived cellulose nanocrystals (CNCs). The use of AFM allows for the unprecedented material characterization of individual CNCs as compared to other methods that can characterize only aggregate properties. Several AFM imaging modes were used to characterize CNCs in terms of topography, adhesion, and stiffness. Using fully 3D finite element methods of tip−CNC indentation, a procedure was developed to calculate the transverse elastic modulus (E_T) from the experimentally measured force−distance data. The influence of relative humidity on the topography, stiffness, and adhesion of CNCs was carefully measured by comparing AFM measurements on the same CNC under different humidity conditions (0.1 and 30% RH). Additionally, AFM nanomanipulations were used to investigate the flexibility of individual CNCs. The following conclusions can be made from this study. Typically, the CNCs produced for this study were 100−300 nm in length and 2−8 nm in height. The height along a given CNC length was not constant, typically undergoing a 2−4 nm change in height. There is also evidence for changes in the in-plane width of the CNC, but this dimension cannot be determined with high accuracy using AFM. The CNC stiffness and adhesion were fairly uniform along the entire CNC length, despite changes in CNC height of 3−8 nm. The measured E_T of 18−50 GPa in nitrogen was within the range predicted by Tashiro and Kobayashi[39] and Jawson,[36] but the associated crystallographic orientation could not be determined. Finally, AFM manipulation results showed CNC bending, but it was unclear if this resulted from single-crystal bending or multiple CNCs pivoting relative to their contact point.

Acknowledgment. We thank the US Forest Services and Discovery Park at Purdue University for funding this project. We are grateful to Pablo Ares from Nanotec Electronica for his continuous assistance with the WSxM software, Rick Reiner of the US Forest Service for processing the cellulose nanocrystals, and Jim Beecher of the US Forest Service for many useful discussions.